ADVANCED HEALTHCARE MATERIALS
www.advhealthmat.de

# A 700 nm LED Light Activated Ru(II) Complex Destroys Tumor Cytoskeleton via Photosensitization and Photocatalysis

*Anyi Dao, Shiyan Chen, Li Pan, Qingyan Ren, Xun Wang, Haorui Wu, Qiufang Gong, Zeduan Chen, Shaomin Ji, Jiaxi Ru, HaoTu Zhu, Chao Liang,* Pingyu Zhang,* Haiping Xia,* and Huaiyi Huang**

**Photoactivable chemotherapy (PACT) using metallic complexes provides spatiotemporal selectivity over drug activation for targeted anticancer therapy. However, the poor absorption in near-infrared (NIR) light region of most metallic complexes renders tissue penetration challenging. Herein, an NIR light triggered dinuclear photoactivable Ru(II) complex (Ru2) is presented and the antitumor mechanism is comprehensively investigated. The introduction of a donor–acceptor–donor (D–A–D) linker greatly enhances the intramolecular charge transition, resulting in a high molar extinction coefficient in the NIR region with an extended triplet excited state lifetime. Most importantly, when activated by 700 nm NIR light, Ru2 exhibits unique slow photodissociation kinetics that facilitates synergistic photosensitization and photocatalytic activity to destroy diverse intracellular biomolecules. In vitro and in vivo experiments show that when activated by 700 nm NIR light, Ru2 exhibits nanomolar photocytotoxicity toward 4T1 cancer cells via the induction of calcium overload and endoplasmic reticulum (ER) stress. These findings provide a robust foundation for the development of NIR-activated Ru(II) PACT complexes for phototherapeutic application.**

## 1. Introduction

Cancer remains a serious global health concern, despite the recent advances in traditional cancer treatments such as chemotherapy, radiotherapy, surgery, and targeted immunotherapies.[1] Photodynamic therapy (PDT) has gained great interest in recent years as a promising approach that can achieve spatiotemporal selectivity and accurate anticancer phototherapy.[2] PDT is an active and non-invasive treatment method in which photosensitizers consume intracellular oxygen, resulting in the production of reactive oxygen species (ROS) that induce cell death.[3] However, the hypoxic microenvironment of solid tumors poses a severe obstacle to PDT effectiveness and is associated with poor patient outcome.[4] To address these problems, Bonnet, Etchenique, Turro, Kodanko, Glazer, Zhu, McFarland, Sadler et al. developed photoactivated chemotherapy (PACT), in which metallic complexes such as Ru(II) or Pt (IV) are employed (**Scheme 1**).[5]

The introduction of a steric hindrance ligand to Ru(II) complexes enables photo-induced ligand dissociation, rendering them suitable for PACT.[6] As the concept of PACT evolves, dual-mode metallic complexes that combine PACT with PDT have shown remarkable potential in targeting hypoxic cancer cells.[7] However, the

A. Dao, L. Pan, H. Wu, H. Huang
School of Pharmaceutical Science (Shenzhen)
Shenzhen campus of Sun Yat-sen University
Shenzhen 510275, China
E-mail: huanghy87@mail.sysu.edu.cn

S. Chen, H. Xia
Shenzhen Grubbs Institute and Department of Chemistry
Southern University of Science and Technology
Shenzhen 518055, China
E-mail: xiahp@sustech.edu.cn

Q. Ren, X. Wang, P. Zhang
College of Chemistry and Environmental Engineering
Shenzhen University
Shenzhen 518060, China
E-mail: p.zhang6@szu.edu.cn

Q. Gong, J. Ru, C. Liang
Institute for Advanced Research
Cixi Biomedical Research Institute
Wenzhou Medical University
Wenzhou, China
E-mail: liangchao@wmu.edu.cn

Z. Chen, S. Ji
Light Industry and Chemical Engineering College Guangdong University of Technology
Guangzhou 510006, China

H. Zhu
Department of Oncology
Seventh Affiliated Hospital of Sun Yat-Sen University
Shenzhen 518107, China

DOI: 10.1002/adhm.202400956

 

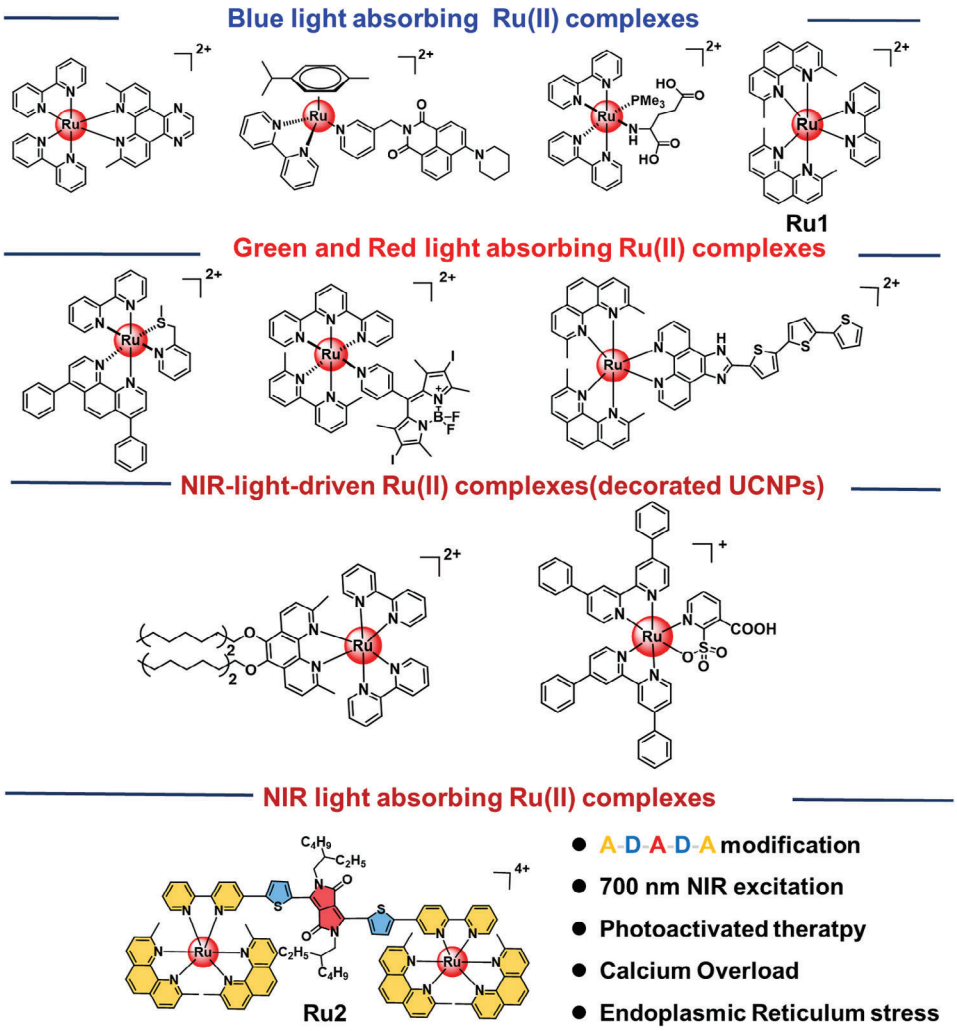


**Scheme 1.** Chemical structure of light triggered Ru(II) complexes for anticancer phototherapy.

investigation of intracellular antitumor mechanisms of action (MoA) lags significantly behind the development of PACT drugs, with only a few reports available in the literature. Glazer and Bonnet discovered covalent modification of ligand and DNA to damage DNA.[5a,i] Kodanko reported cathespin B inhibition by photoactivated Ru(II) complex.[8] Thus it is important to discover novel intracellular MoA to promote the development of PACT agents. Recently, we and others have reported photocatalytic anticancer therapy with metal complexes, providing an additional modality to treat hypoxic tumor.[9]

The three-dimensional structures and readily modification of chelated ligands of Ru(II) complexes allow for structure–activity relationship (SAR) investigation.[10] However, most of the reported Ru(II) PACT complexes suffer from extremely weak absorption in the near infrared (NIR), limiting the tissue penetration of phototherapy.[11] Thus, there is an urgent need to develop NIR-light activated Ru(II) PACT complexes. Recently, extending the ligand delocalization effect with donor–acceptor–donor (D–A–D) have been discovered as a promising strategy to enhance the NIR absorption of metal complexes.[12] In addition, D–A–D materials can change the excited state properties of metal complexes and significantly prolong the excited state lifetime.[13] However, Ru(II) PACT agents modified with D–A–D materials and the potent intracellular MoA have not yet been reported before.

Hence, we combined photoactivable Ru(II) complex (**Ru1**) with 2,5-bis(2-ethylhexyl)−3,6-di(thiophen-2-yl)pyrrolo[3,4-c]pyrrole-1,4 (2*H*,5*H*)-dione (D–A–D moiety) to develop a novel dinuclear Ru(II) complex (**Ru2**) as NIR-light activated PACT agents. **Ru2** exhibited absorption at the NIR phototherapeutic window, long triplet excited state lifetime. Upon exposure to 700 nm LED light, **Ru2** showed slow ligand dissociation activity with photosensitization activity. Importantly, **Ru2** showed the nanomolar photocytotoxicity toward 4T1 cells, the triple negative breast cancer (TNBC) in vitro and in vivo, when exposed to 700 nm NIR light. The treatment strategy for TNBC remains a major unmet need, due to its aggressive and poor prognosis, with chemotherapy being the only therapeutic option in clinic.[14] Intracellular anticancer MoA studies revealed that **Ru2** induced intracellular redox imbalance via endoplasmic reticulum (ER) stress in 4T1 cells, following calcium overload and tubulin polymerization inhibition.

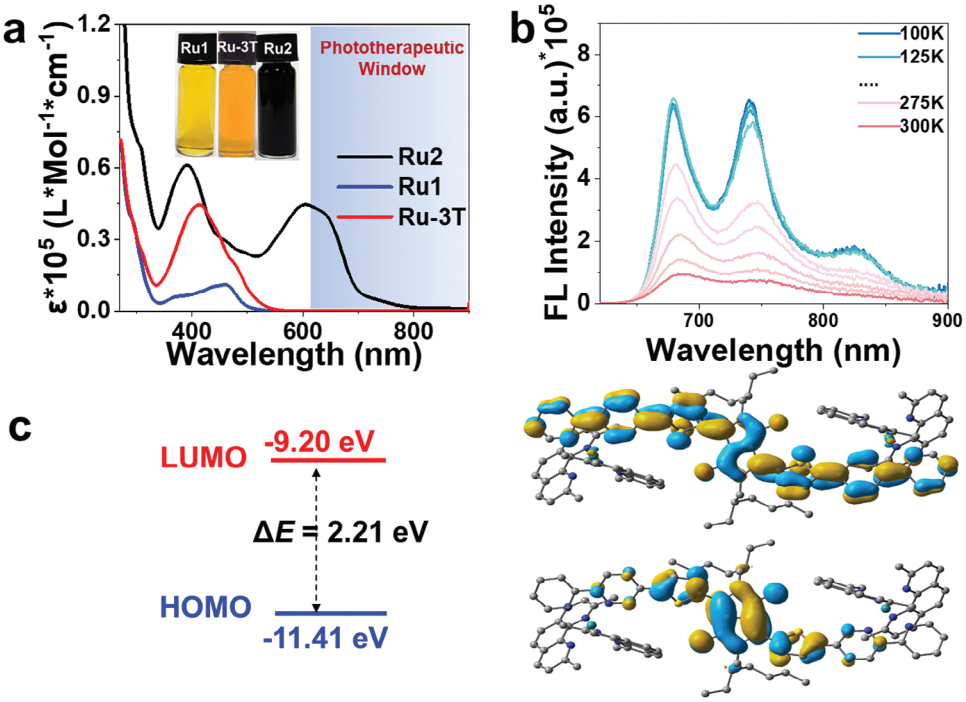


**Figure 1.** Photophysical property and computational studies. a) UV–vis absorption spectra of Ru(II) complexes ($10 \times 10^{-6}$ M) in DCM. b) Temperature dependent emission spectra of **Ru2** ($10 \times 10^{-6}$ M) (dissolved in a solution of $V_{ethanol}$:$V_{methanol}$ = 4:1). c) Frontier molecular orbitals and energies (eV) from DFT calculations of **Ru2** in their ground state ($S_0$).

## 2. Results and Discussion

### 2.1. Synthesis and Photoproperty Studies

The mono- and dinuclear **Ru1** and **Ru2** complexes (Scheme 1; Figure S1, Supporting Information) were presented together with and their respective synthetic procedures in the Supporting Information. A synthetic version of the mononuclear complex **Ru1** and **Ru3T** were prepared for the SAR experiment.[15] The dinuclear complex (**Ru2**) was synthesized via Stille coupling reaction with brominated **Ru1** with the trimethylstannyl D–A–D linker (Figure S1, Supporting Information) in toluene/DMF (V/V = 1:1). **Ru2** and **Ru3T** was characterized by $^{1}$H and $^{13}$C nuclear magnetic resonance, high-resolution mass spectrometry, and high-performance liquid chromatography (Figures S2–S8, Supporting Information). Importantly, **Ru2** exhibited a much higher molar extinction coefficient ($\epsilon$) covering 600–800 nm region compared with the traditional mononuclear complex **Ru1** and **Ru3T** (**Figure** 1a; Figure S9, Supporting Information). Thus, a significant bathochromic shift was achieved for **Ru2** due to the introduction of D–A–D linker.

The excited-state electronic and photophysical properties of **Ru2** were investigated using density functional theory (DFT) and time-dependent DFT (TD-DFT). The steric hindrance effect of 2,9-dimethyl-1,10-phenanthroline (dmp) ligand led to disordered octahedral geometries of the ground-state singlet of Ru(II) metal complexes (Figure S10, Supporting Information). In sharp contrast to the metal-to-ligand charge transfer ($^{1}$MLCT) in **Ru1**, **Ru2** exhibited typical intra-ligand charge transfer ($^{1}$ILCT) as a result of the delocalization of the HOMO and LUMO orbitals of the linker (Figure 1c; Figure S11, Supporting Information), similar to Ru-3T.[15] The absorption maximum of **Ru2** was calculated to be 608 nm, of which 97.4% was attributed to increased oscillator strength ($f$ = 1.0072) (Table S1, Supporting Information), and consistency was observed between the calculated and experimental absorption band (Figure S12, Supporting Information). **Ru2** (2.21 eV) exhibited NIR absorption as compared to **Ru1** (3.37 eV) because of the lower HOMO–LUMO gap, which facilitated electron transport at the excited state. The theoretical properties of **Ru2** were then compared to those of other photoactivated Ru(II) complexes, with the results presented in **Table** 1. The addition of a D–A–D linker was found to successfully shifted the absorption spectrum of the Ru(II) complex into the NIR region, appealing for deep tissue anticancer phototherapy.

For most of the Ru(II) PACT agents, the activation of metal-centered state completely quenched the emission, such as **Ru1** and **Ru3T** (Figure S13, Supporting Information), **Ru2** exhibited a unique NIR emission at room temperature (Figure S14, Supporting Information). Moreover, the luminescence intensity of **Ru2** increased in high viscosity (glycerinum, Figure S15, Supporting Information) and hydrophobic ($CH_2Cl_2$, quantum yield 2%, Figure S16, Supporting Information) solvents, indicating the potential for excited state photoreactivity within cancer cells.[9b] However, oxygen had no effect on the emission intensity of **Ru2**, indicating fluorescence nature at room temperature (Figure S17, Supporting Information). To validate this hypothesis, a temperature-dependent luminescence test (Figure 1b; Figure S18, Supporting Information) was conducted. Interestingly, two emission peaks at 742 and 825 nm appeared

**Table 1.** Photoproperties of Ru(II) complexes in dichloromethane.

| Ru(II) Complexes | log $\epsilon$ [nm] | PL [nm] | $\varphi$ [%] | $\tau_{TA}$ [μs] | $T_1$-$S_0$ [eV] | HOMO–LUMO [eV] |
|---|---|---|---|---|---|---|
| **Ru1** | 290(4.60) 462(4.05) | n.d. | n.d. | n.d. | 2.15 | 3.37 |
| **Ru2** | 600(4.54) 700(3.94) | 692(300 K)742(100 K) | 2% | 1.6 | 0.97 | 2.21 |
| **Ru-3T** | 477(4.38) 600 (1.91) | n.d. | n.d. | 25[a)] | 1.87[a)] | 3.15[a)] |

n.d. = Not detected; PL = Photoluminescence; $\varphi$ = fluorescence quantum yield; $\tau_{TA}$ = triplet excited state lifetime; [a)] data from reference.

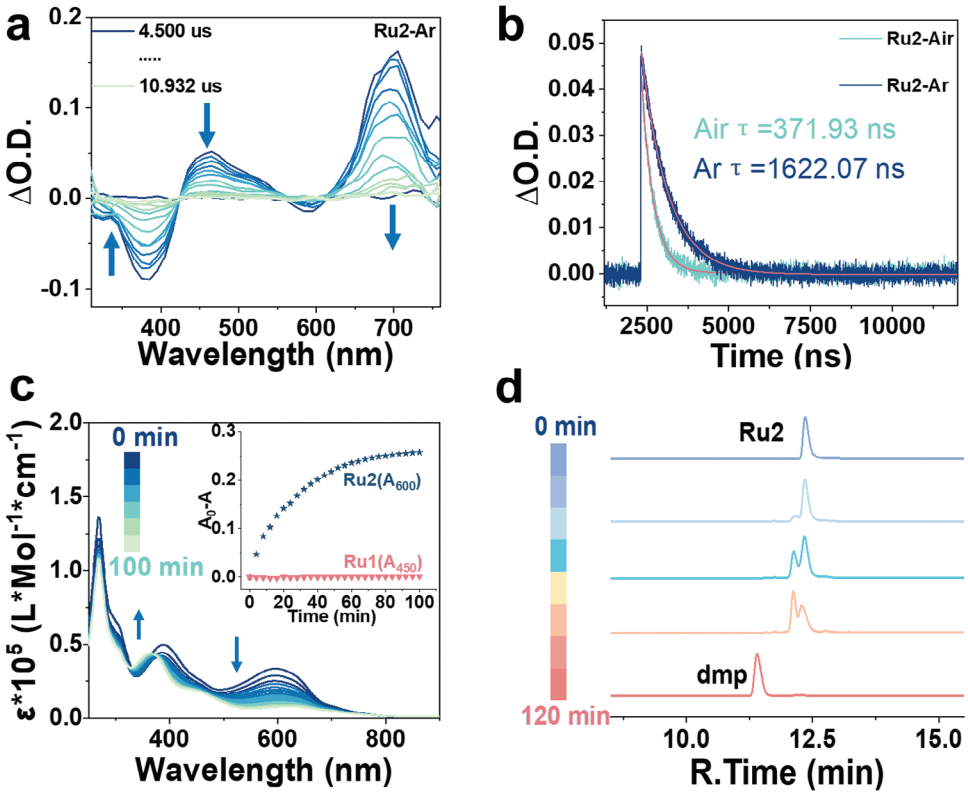


**Figure 2.** Excited state and photoactivation properties of **Ru2**. a) TA absorption spectra of **Ru2** at 298 K. b) Triplet excited state lifetime of **Ru2** ($10 \times 10^{-6}$ M) in DCM at 298 K, $\lambda_{ex}$ = 600 nm. c) UV–vis absorption spectra change of **Ru2** ($10 \times 10^{-6}$ M) after 700 nm light illumination (285 J $cm^{-2}$) in PBS. Insert: comparison of ligand dissociation rate of **Ru1** and **Ru2** in PBS. d) HPLC traces of **Ru2** ($10 \times 10^{-6}$ M) in $CH_3OH$ before and after 700 nm light treatment (285 J $cm^{-2}$).

as the temperature was decreased from 300 to 100 K. The photophysical characteristics were summarized in Table 1. Overall, the introduction of the D–A–D linker allowed the construction of Ru(II) complex with appealing NIR absorption/emission.

Nanosecond transient absorption (TA) was further used to investigate and elucidate the triplet excited state properties. As shown in **Figures** 2a and S19 (Supporting Information), the ground state bleaching (GSB) bands were centered near 390 nm, and the characteristic bands matched the UV–vis spectra well. Two regions of excited state absorption (ESA) bands were observed in the TA spectra. The region between 425 and 560 nm corresponded to the triplet metal-to-ligand charge transfer ($^3$MLCT), while the ESA band between 610 and 750 nm can be attributed to the triplet intraligand charge transfer ($^3$ILCT) that originated from the linker. The triplet excited-state lifetime of **Ru2** was estimated to be 371 ns in air and 1622 ns under argon atmosphere, based on the decay trace observed at the 470 nm GSB band (Figure 2b). Notably, the sharply different triplet state lifetimes under normoxia and Ar indicated an excited-state interaction with oxygen.

The absorption properties of **Ru2** inspired investigation of the NIR light activation properties. Surprisingly, **Ru2** exhibited an obvious change in the absorption spectrum with a distinct hypochromic shift upon excitation with 465 nm light (Figure S20, Supporting Information), which differed significantly from bathochromic-shift of **Ru1** and **Ru3T** (Figure S21, Supporting Information). Under 700 nm light activation, **Ru2** demonstrated a ligand dissociation kinetic that was induced by NIR light, with a slow dissociation process. The isosbestic point appeared at 380 nm indicating formation of new species, while **Ru1** remained unchanged under identical conditions (Figure 2c; Figure S22, Supporting Information). The kinetic rate of ligand dissociation can be quantified by photosubstitution quantum yield ($\Phi_{ps}$).[15]

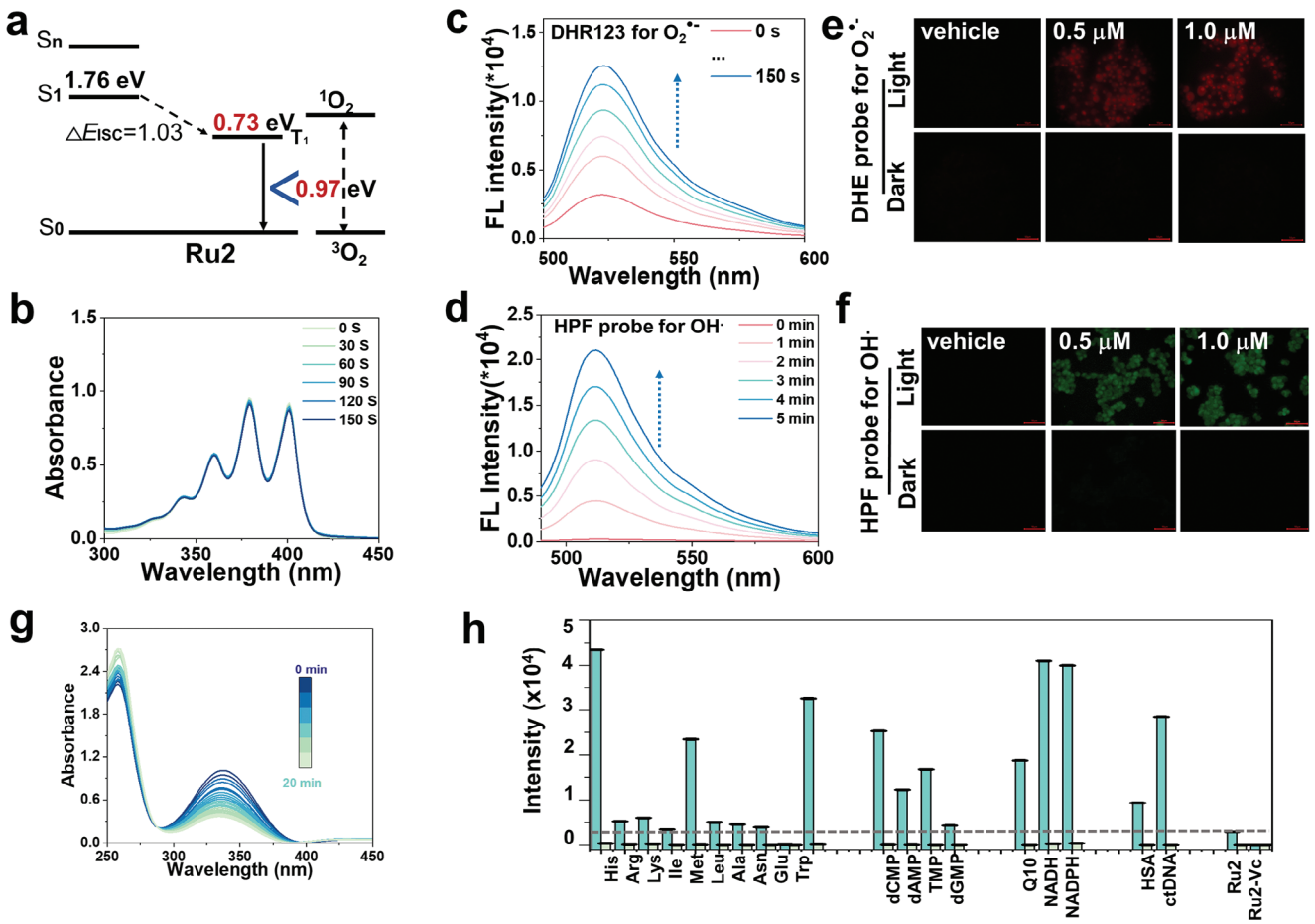


**Figure 3.** Photosensitization and photocatalytic activity of **Ru2** in PBS and in cancer cells. a) The possible photophysical processes reflected by the calculated lowest excited singlet ($S_1$) and triplet energy ($T_1$) levels of **Ru2**. b) $^1O_2$ generation efficiencies of **Ru2** ($5 \times 10^{-6}$ M) after illumination (700 nm, 7.1 J cm$^{-2}$). c) $O_2^{\bullet-}$ generation of **Ru2** ($5 \times 10^{-6}$ M) in PBS (700 nm, 7.1 J cm$^{-2}$). d) OH$^\bullet$ generation by **Ru2** ($5 \times 10^{-6}$ M) in PBS (700 nm, 14.3 J cm$^{-2}$). e) Intracellular $O_2^{\bullet-}$ generation by **Ru2** (0.5 and $1 \times 10^{-6}$ M), scale bar: 50 μm. f) Intracellular OH$^\bullet$ generation by **Ru2** (0.5 and $1 \times 10^{-6}$ M), scale bar: 50 μm. g) The photocatalytic oxidation of NADPH ($160 \times 10^{-6}$ M) by **Ru2** ($5 \times 10^{-6}$ M) in aqueous solution under 700 nm irradiation (57 J cm$^{-2}$). h) Photocatalytic $H_2O_2$ generation of **Ru2** ($10 \times 10^{-6}$ M) in the presence of biomolecules, the experimental data were presented as mean ± SD ($n = 3$).

The $\Phi_{ps}$ of **Ru2** was calculated to be 0.0022%, 236 times smaller than Ru-3T (0.52%).[15] The slow dissociation of **Ru2** may contribute to the production of ROS and its photocatalytic oxidation ability at the excited state.[15]

The light-triggered ligand dissociation properties of **Ru2** were further investigated by HPLC and mass spectrometry. In the absence of light, **Ru2** appeared as a solo peak on the HPLC at 12.36 min, while the dmp ligand appeared at 11.39 min. As the irradiation time progressed, the peak of **Ru2** decreased gradually, with a new peak appearing at 11.91 min (Figure 2d). Comparing the two peaks in the UV–vis absorption spectra may lead to the conclusion that the dmp ligand was only partially dissociated from **Ru2** (Figure S23, Supporting Information) after NIR light treatment. Similarly, two new mass peaks 483.0 ($[M+2CH_3O^-+H^+]^{3+}$) and 643.8 ($[M+2CH_3O^-]^{4+}$) were detected by mass spectrometry (Figure S24, Supporting Information), confirming that **Ru2** underwent partially decompose. However, dmp ligand did not completely dissociate.

### 2.2. Photosensitization and Photocatalysis Studies

Previously, Glazer and McFarland verified that Ru(II) PACT complexes with long triplet excited state lifetime and slow ligand dissociation rate could enhance photosensitization activity.[5b] The characteristics of **Ru2**, including slow ligand dissociation in the presence of NIR radiation and prolonged triplet excited state lifetime, may enhance the photosensitization and photocatalytic activity of **Ru2**. TDDFT calculations revealed that the energy disparity between the triplet ($T_1$) and ground state ($S_0$) of **Ru2** (0.73 eV) was lower than that of the $^3O_2/^1O_2$ energy gap (0.97 eV) (**Figure 3a**), suggesting that electron transfer rather than energy transfer pathway was likely to dominate the excited state reaction. To support this hypothesis, the generation efficiency of singlet oxygen ($^1O_2$), superoxide anion ($O_2^{\bullet-}$), and hydroxyl radical (OH$^\bullet$) was conducted.[16] In line with the calculation results, **Ru2** can only induced slightly photo depletion of $^1O_2$ indicator ABDA (9,10-anthracenediyl-bis(methylene)dimalonic Acid (Figure 3b; Figure S25, Supporting Information). In contrast, the fluorescence

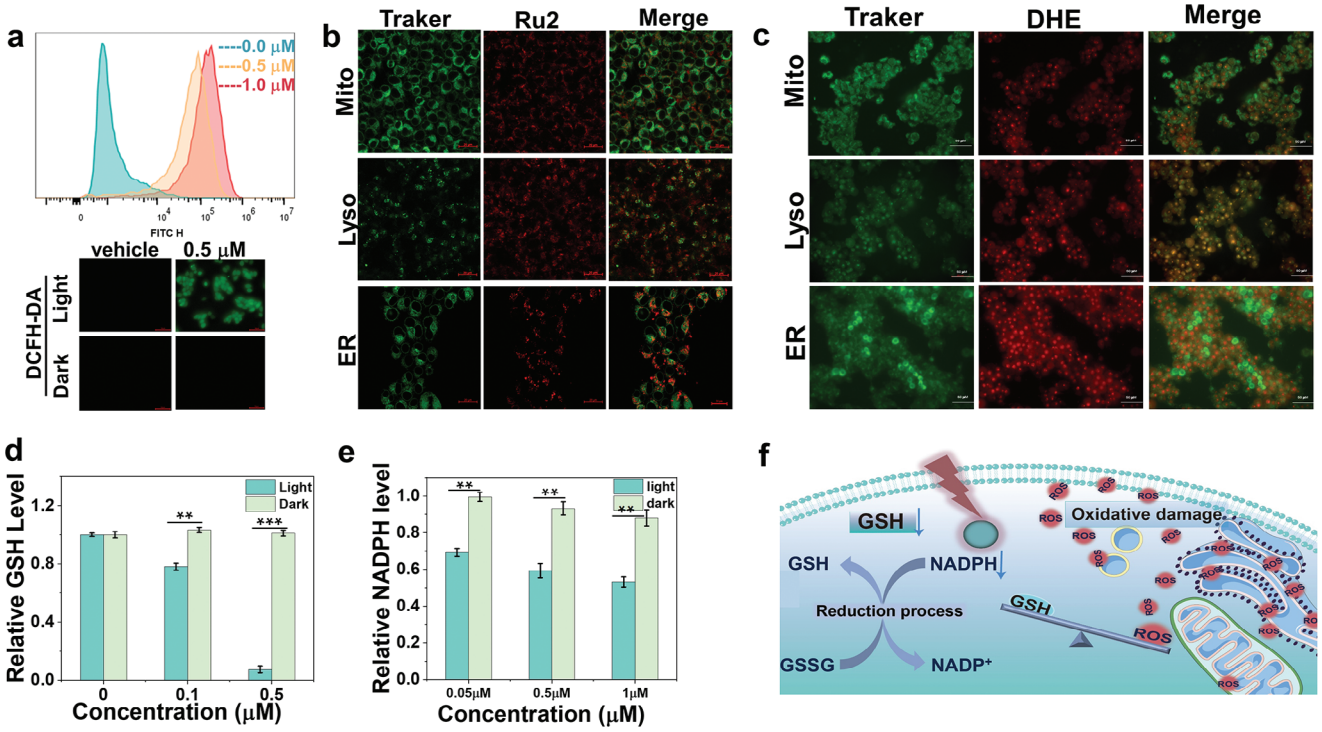


**Figure 4.** ROS generation and GSH depletion of **Ru2** in 4T1 cancer cells. a) ROS production in 4T1 cells treated by **Ru2** ($0.5 \times 10^{-6}$ M) after 700 nm light treatment (99.6 J $cm^{-2}$). b) Intracellular localization of **Ru2** ($20 \times 10^{-6}$ M) in 4T1 cells, costained with Mito-tracker, ER-tracker, and Lyso-tracker dyes. ($E_x/E_m$ for **Ru2** was 633 nm/700 ± 50 nm, $E_x/E_m$ for Lyso-, ER-and Mito- Tracker was 488 nm/550 ± 50 nm) Scale bar: 20 μm. c) Mitochondria, lysosome, and ER damage induced by **Ru2** ($0.1 \times 10^{-6}$ M) via superoxide anion generation after 700 nm light treatment (99.6 J $cm^{-2}$). Scale bar: 50 μm. d) Intracellular GSH levels of 4T1 cells treated with **Ru2** (0.1 and $0.5 \times 10^{-6}$ M) after 700 nm light treatment (99.6 J $cm^{-2}$). e) Intracellular NADPH levels of 4T1 cells treated with **Ru2** (0.05, 0.5, and $1 \times 10^{-6}$ M) after 700 nm light treatment (99.6 J $cm^{-2}$). f) Schematic diagram of oxidative damage by photoactivation of **Ru2**. The experimental data were presented as mean ± SD ($n = 3$). Statistical significance was calculated with two-tailed Student's $t$ test (***$p < 0.001$, **$p < 0.01$, or *$p < 0.05$).

intensity of the $O_2^{\bullet-}$ indicator DHR123 (dihydrorhodamine 123) increased sixfold only after 150 s of 700 nm light treatment, (Figure 3c). The fluorescence intensity of the $OH^{\bullet}$ indicator hydroxyphenyl (HPF, Figure 3d; Figure S26, Supporting Information) was also enhanced after light treatment. Moreover, intracellular ROS signal was also detected in 4T1 cancer cells after 700 nm light treatment. The intracellular fluorescent signal of DCFH-DA (ROS indicator, **Figure** 4a), superoxide anion probe DHE (Figure 3e), and $OH^{\bullet}$ probe HPF (Figure 3f) confirmed that **Ru2** showed typical Type-I NIR light-activated photosensitization, rendering attractive for PDT under hypoxic condition.

The electron transfer capability of **Ru2** led us to further investigation of photocatalytic activity, with particular focus on the efficiency of diverse intracellular biomolecules. Recently, the intracellular coenzyme II, NADPH, a crucial component of both cellular biosynthesis and the antioxidant system, has gained significant interest as a target for photoredox catalytic therapy. As shown in Figure 3g, **Ru2** treated with 700 nm light exhibited NADPH oxidation photocatalytic activity, with turnover frequencies (TOFs) of 61 $h^{-1}$. In addition, the robust photocatalytic activity of **Ru2** toward the intracellular substrates in buffer solution was determined by measuring the efficiency of $H_2O_2$ generation (Figure 3h; Figure S27, Supporting Information). In the presence of histidine, methionine, tryptophan, tyrosine, and lysine, **Ru2** induced high $H_2O_2$ generation when exposed to 700 nm light, indicating its catalytic ability toward common amino acids. In addition, **Ru2** also exhibited photocatalytic activity toward nucleosides, coenzymes, and proteins, including human serum albumin (HSA) (Figure 3h).

### 2.3. 700 nm NIR LED Light Triggered Anticancer Activity

The appealing excited state reactivity of **Ru2** promoted us to evaluate the NIR light-activated anticancer activity under both normoxic (21% $O_2$) and hypoxic (1% $O_2$) conditions. Four cancer cell lines were selected for this study, including A549 (human lung cancer), A549/DDP (cisplatin-resistant A549), 4T1 (mouse breast cancer), and MCF-7 (human breast cancer). As shown in **Table** 2 and Figure S27 (Supporting Information), the dark $IC_{50}$ value of **Ru2** was between 10.5 and $23.1 \times 10^{-6}$ M after 48 h incubation in the dark. Notably, the photocytotoxicity of **Ru2** enhanced significantly when exposed to 700 nm light (99.6 J $cm^{-2}$), while **Ru-3T** was totally inactive under the same conditions. Under normoxia (21% $O_2$) and 700 nm light activation, **Ru2** exhibited nanomolar light $IC_{50}$ values ($IC_{50} = 0.02–0.06 \times 10^{-6}$ M) and a phototherapeutic index (PI) reaching as high as 637. **Ru2** remained active even under hypoxic conditions (1% $O_2$), with $IC_{50}$ values as low as $0.6 \times 10^{-6}$ M, which was an order of magnitude lower than the clinical anticancer drug, cisplatin. However, under 700 nm

**Table 2.** Dark and light $IC_{50}$ ($10^{-6}$ M) and PI (phototoxicity index) values towards various cancer cell lines.

| | Under normoxic condition (21% $O_2$) | | | | | | | | | | | |
|---|---|---|---|---|---|---|---|---|---|---|---|---|
| Cell lines | 4T1 | | | MCF-7 | | | A549 | | | A549/DDP | | |
| Complexes | Dark[a] | Light[b] | PI[c] | Dark[a] | Light[b] | PI[c] | Dark[a] | Light[b] | PI[c] | Dark[a] | Light[b] | PI[c] |
| **Ru2** | 10.5 ± 1.1 | 0.02 ± 0.008 | 525 | 19.1 ± 2.1 | 0.03 ± 0.004 | 637 | 22.9 ± 1.9 | 0.04 ± 0.009 | 573 | 23.1 ± 1.3 | 0.06 ± 0.002 | 385 |
| **Ru-3T** | 14.3 ± 2.2 | 13.1 ± 1.4 | 1 | 69.1 ± 2.5 | 51.1 ± 1.7 | 1 | 26.3 ± 1.8 | 25.1 ± 2.9 | 1 | 64.5 ± 1.1 | 63.1 ± 3.2 | 1 |
| Cisplatin | 10.9 ± 1.9 | 11.5 ± 1.4 | 1 | 16.1 ± 1.1 | 15.1 ± 0.7 | 1 | 3.10 ± 0.3 | 3.11 ± 0.5 | 1 | 87.1 ± 2.1 | 93.1 ± 1.7 | 1 |
| | Under hypoxic condition (1% $O_2$) | | | | | | | | | | | |
| | 4T1 | | | MCF-7 | | | A549 | | | A549/DDP | | |
| | Dark[a] | Light[b] | PI[c] | Dark[a] | Light[b] | PI[c] | Dark[a] | Light[b] | PI[c] | Dark[a] | Light[b] | PI[c] |
| Ru2 | 11.0 ± 2.4 | 0.9 ± 0.1 | 12 | 21.3 ± 2.2 | 0.8 ± 0.09 | 27 | 8.7 ± 1.4 | 0.9 ± 0.07 | 10 | 23.3 ± 2.1 | 0.6 ± 0.1 | 39 |
| Ru-3T | 11.1 ± 1.3 | 10.2 ± 1.2 | 1 | 68.1 ± 3.2 | 52.1 ± 2.6 | 1 | 28.8 ± 2.9 | 26.2 ± 2.5 | 1 | 67.1 ± 3.3 | 64.2 ± 1.8 | 1 |
| Cisplatin | 15.5 ± 1.3 | 11.1 ± 0.9 | 1 | 12.3 ± 1.8 | 14.1 ± 2.1 | 1 | 3.23 ± 0.7 | 4.21 ± 0.1 | 1 | >100 | >100 | n.a.[d] |

[a] 48 h drug exposure; [b] 6 h drug exposure, then received 700 nm (99.6 J $cm^{-2}$) irradiation without changing the medium, following 42 h incubation in the dark; [c] PI = $IC_{50}$(Dark[a]) / $IC_{50}$(Light[b]); [d] n.a. = not applicable. The experimental data were presented as mean ± SD ($n = 3$).

NIR light excitation, **Ru-3T**, one of the most active Ru(II) PACT agents, the PI values were close to 1 for all four cell lines normal normoxia or hypoxic conditions. This result was due to the extremely low absorption ability of **Ru-3T** at the NIR region. Thus, the enhanced NIR light absorption property and high excited electron transfer efficiency of **Ru2** resulted in photocytotoxicity activity toward cancer cells under 700 nm NIR light activation. Since **Ru2** was active toward 4T1 cancer cells, the triple negative breast cancer (TNBC) cell line, which currently chemotherapy is only available with poor prognosis in clinic. Considering the promising NIR light triggered cytotoxicity induced by **Ru2**, the mechanism of action (MoA) was further investigated in 4T1 cells.

### 2.4. Anticancer Mechanism Studies

Considering the fact that **Ru2** effectively stimulated intracellular ROS production (Figure 4a). Thus, flow cytometry was further used to quantify the intracellular ROS production. Interestingly, it was observed that, when exposed to 700 nm light, **Ru2** induced a significant increase in ROS levels under normoxic conditions (Figure 4a). Thus, oxidative damage MoA may contribute to the anticancer effect.

Confocal laser scanning microscopy and co-staining with fluorescence organelle trackers were used to examine the cellular localization of **Ru2** within 4T1 cancer cells. In contrast to the previously reported upon photoactivated Ru(II) complexes that target the nucleus, it was discovered that **Ru2** was predominantly localized within the cytoplasm.[5i] The Figure 4b demonstrates partial overlap between the red signal representing **Ru2** and the green fluorescent signal that indicated the presence of lysosome and ER trackers. Treatment with 700 nm light led to significant organelle damage as a result of the superoxide anion, as indicated by the combined signals for organelle dyes and the superoxide anion dye DHE (Figure 4c), indicating intracellular oxidative damage.

To protect against oxidative damage, the intracellular antioxidative system (high concentration of ROS-scavenger glutathione (GSH)) is likely to reduce the efficiency of PDT.[17] Therefore, depleting the high levels of GSH in tumor cells may be a crucial step in efficient phototherapeutic activity. In addition, as mentioned above, **Ru2** can catalyze the oxidation of NADPH, the essential coenzyme in the glutathione reductase system that regenerates GSH from glutathione disulfide (GSSG), **Ru2** may remain active via oxidation of GSH by ROS production and NADPH depletion. Thus, the intracellular concentration changes of GSH and NADPH after exposure to light and **Ru2** was investigated. **Ru2** showed no significant influence on cellular GSH (Figure 4d) or NADPH (Figure 4e) in the dark. However, **Ru2** consumed significant amounts of the intracellular NADPH and GSH in 4T1 cancer cells after NIR treatment via PDT, and photocatalytic anticancer therapy activity. Thus, **Ru2** induced significant oxidative damage to organelles and destroyed the cellular antioxidant system by depleting both NADPH and GSH (Figure 4f). Furthermore, it is anticipated that, in addition to GSH-depleting, NADPH-photocatalytic oxidation, and partial ER localization properties, **Ru2** may interact with the free mercapto group in primary proteins, inhibiting their participation in the protein modification process in the ER. **Ru2** may also inhibit the sulfhydryl/disulfide bond conversion that is catalyzed by the NADPH-dependent redox enzymes.[17] ER is the primary calcium reservoir in living cells and plays a crucial role in calcium homeostasis.[18] Calcium fluorescence imaging (**Figure 5**a) and flow cytometry (Figure 5b) revealed that oxidative ER damage and NADPH photocatalysis were induced by **Ru2**, increasing the cytoplasmic calcium levels. ER damage and calcium leakage can induce ER stress in living cells. Western blot analysis was thus used to determine whether **Ru2** induces ER stress within 4T1 cells. The mammalian ER stress pathway is regulated by three transmembrane receptor proteins, and a shift in the BIP expression is an indicator of ER stress.[19] The Figure 5c showed the significant increase in the expression of the BIP protein in 4T1 cells treated with light and **Ru2**, indicating ER stress. In addition, the intracellular expression of CHOP and Casepase-12 also increased (Figure 5c). CHOP is an essential component of the ER stress-mediating apoptosis pathway, with the dissociation of

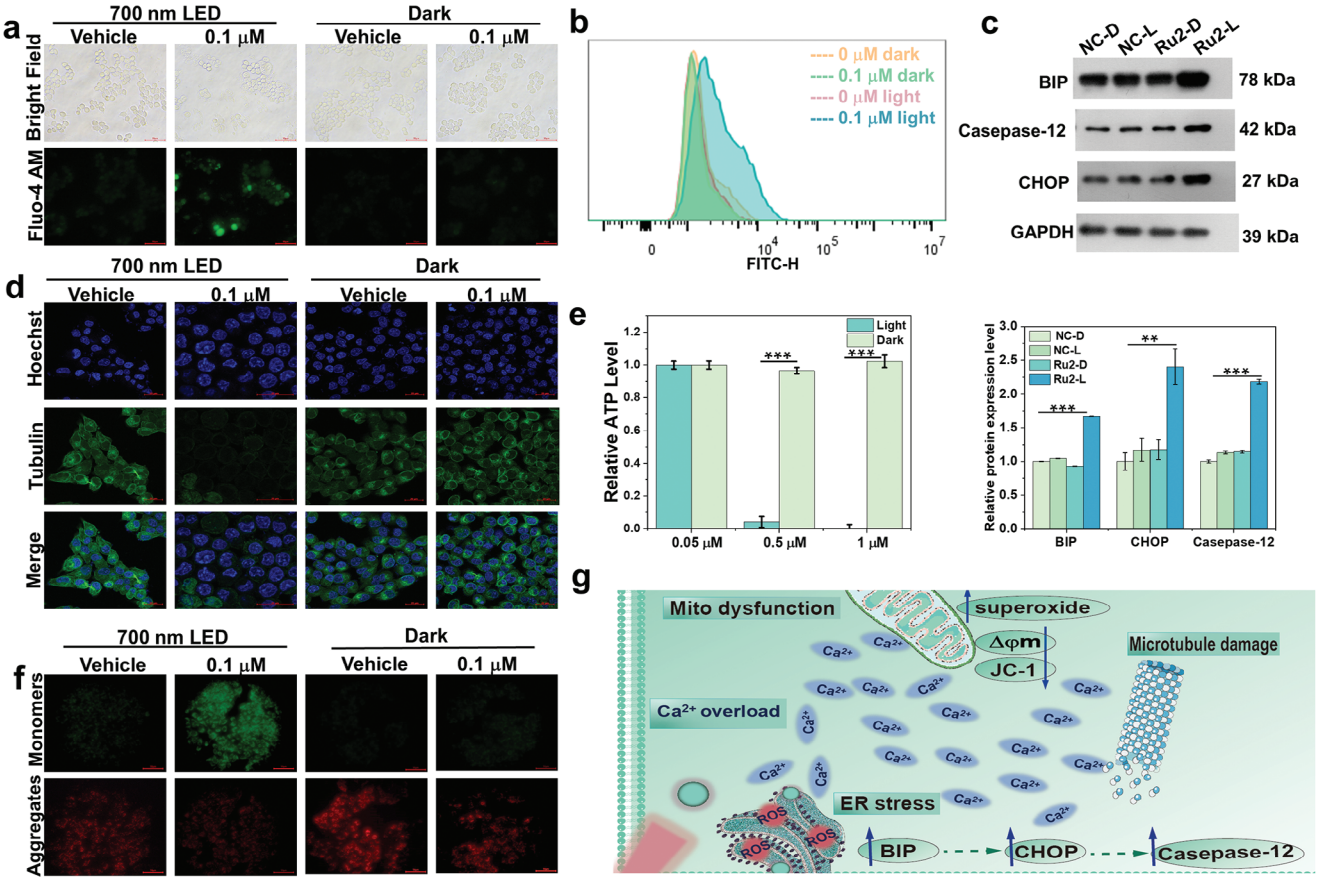


**Figure 5.** **Ru2** induced calcium overload and ER stress in 4T1 cancer cells. a) Intracellular calcium fluorescence imaging monitored by Fluo-4 AM after illumination (700 nm, 99.6 J $cm^{-2}$) in 4T1 cells, scale bar: 50 μm, **Ru2**: $0.1 \times 10^{-6}$ M. b) Flow cytometry of intracellular calcium concentration, **Ru2**: $0.1 \times 10^{-6}$ M. c) Expression of ER stress related proteins by western blotting assay, **Ru2**: $0.1 \times 10^{-6}$ M. Statistical significance was calculated with two-tailed Student's *t* test (***$p < 0.001$, **$p < 0.01$, or *$p < 0.05$). d) Microtubule imaging using Tubulin-tracker green costaining with Hoechst 33 342 in 4T1 cells. ($E_x/E_m$ for Hoechst 33 342 was 405 nm/450 ± 30 nm, $E_x/E_m$ for Tubulin-Tracker Green was 488 nm/540 ± 30 nm, **Ru2**: $0.1 \times 10^{-6}$ M). e) Relative ATP concentration within 4T1 cells treated with **Ru2** (0.05, 0.5, and $1 \times 10^{-6}$ M). The experimental data were presented as mean ± SD ($n = 3$). Statistical significance was calculated with two-tailed Student's *t* test (***$p < 0.001$, **$p < 0.01$, or *$p < 0.05$). f) Mitochondrial membrane potential change induced by **Ru2** ($0.1 \times 10^{-6}$ M) in 4T1 cells. Scale bar: 50 μm. g) Schematic diagram of photoactivated anticancer activity of **Ru2**.

stress protein receptors from BIP resulting in amplified CHOP gene expression during ER stress.[19] Simultaneously, Casepase-12 activates Caspase-3, initiating the apoptotic cascade that ultimately results in cell apoptosis.[20] Overall, the western blot assays revealed that **Ru2** induced ER stress in 4T1 cells following light treatment.

As known, the calcium concentration regulates the polymerization and depolymerization of tubulin dimers. ER stress and excess calcium can also affect the cytoskeleton in terms of stability.[21] As shown in Figure 5d, **Ru2** significantly inhibited tubulin polymerization, resulting in the disappearance of the intracellular microtubule structure after light treatment. However, tubulin was clearly observable in the dark. Moreover, excess cytoplasmic calcium can lead to mitochondrial dysfunction.[21] Using the MitoSOX probe (Figure S29, Supporting Information), an enhancement of superoxide signal within mitochondria was detected together with significant decrease in the intracellular ATP concentrations (Figure 5e). As a result, a significant depletion of mitochondrial membrane potential (Figure 5f) was observed after light treatment in the presence of **Ru2**, indicating an early step in cell apoptosis. Annexin V-FITC and propidium iodide (PI) assays (Figure S30, Supporting Information) further confirmed the apoptosis mechanism. In the absence of light, cancer cells that were treated with **Ru2** exhibited no fluorescence. However, exposure to 700 nm light caused a significant number of 4T1 cells to undergo late-stage apoptosis, as validated using flow cytometry (Figure S31, Supporting Information). Overall, **Ru2** disrupted the intracellular redox homeostasis, induced ER stress-mediated cell apoptosis, and ultimately exhibited photocytotoxicity (Figure 5g, Supporting Information).

### 2.5. In Vivo Photocytotoxicity in 4T1 Mice

Based on the appealing photocytotoxicity toward cancer cells of **Ru2**, a mouse model bearing a 4T1 tumor was further used to investigate the antitumor phototherapeutic efficacy in vivo, for which the unique NIR-excited mode of action was exploited. The lethal dosage ($LD_{50}$) that was calculated for intravenously-administered **Ru2** was 37.7 μg per mouse (18.65 mg $kg^{-1}$) (**Figure**

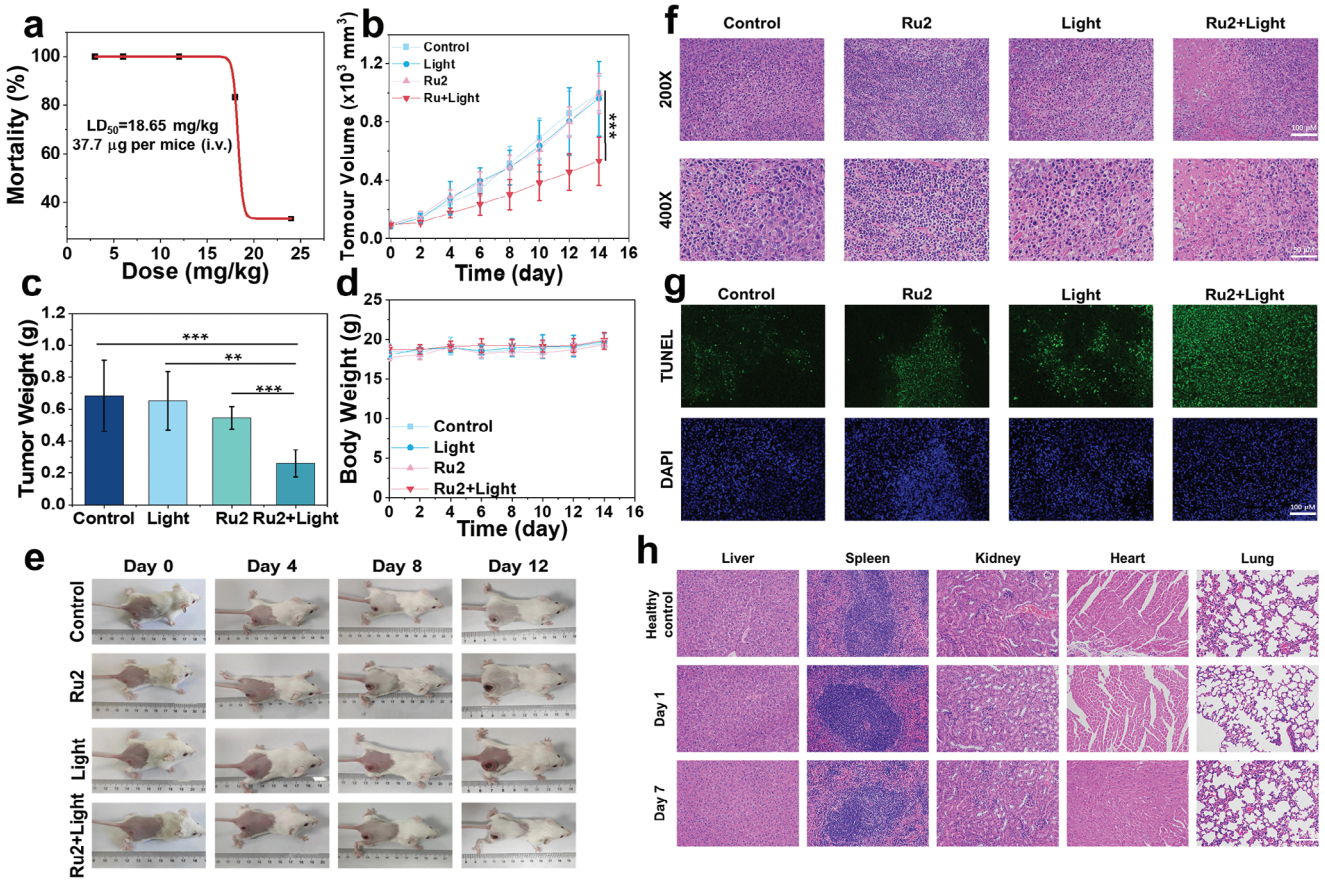


**Figure 6.** In vivo antitumor phototherapy efficiency of **Ru2**. a) In acute toxicity experiment of **Ru2**, each injection dose was investigated in six mice. b) Tumor growth curves of mice after various treatments. The experimental data were presented as mean ± SD ($n = 5$). Statistical significance was calculated with One-way ANOVA method (***$p < 0.001$, **$p < 0.01$, or *$p < 0.05$). c) Average tumor weights of mice at 14 d post various treatments. The experimental data were presented as mean ± SD ($n = 5$). Statistical significance was calculated with One-way ANOVA method (***$p < 0.001$, **$p < 0.01$, or *$p < 0.05$). d) Body weight curves of mice after various treatments. The experimental data were presented as mean ± SD ($n = 5$). e) Photos of representative mice in each group at different time points after various treatments. f,g) Microscopy photos of H&E (f) and TUNEL (g) stained tumor slices. Tumors tissue were collected from mice at 24 h post various treatments. The experiment was repeated three times independently with similar results. Scale bar: 100 μm. h) Microscopy photos of H&E stained main organs slices. Scale bar: 100 μm.

6a). Since **Ru2** does not functionalize with tumor targeting moiety, in this work intratumoral injection is used to verify the in vivo antitumor efficiency. During in vivo antitumor phototherapeutic experiment, 4T1 tumor-bearing mice were randomly distributed into four groups ($n = 5$): (1) Untreated; (2) **Ru2** alone (i.t. injection 6 μg); (3) light alone (700 nm, 99.6 J cm$^{-2}$); (4) **Ru2** + light (i.t. injection 6 μg; 700 nm, 99.6 J cm$^{-2}$). Mice were observed for 14 d after various therapeutic strategies. No significant difference was observed in the growth rate or final volume of 4T1 tumors in the dark control, dark treatment with **Ru2** (6 μg per mouse), and light control groups, as seen in Figure 6b,c,e. However, tumor growth was significantly inhibited in the **Ru2** and 700 nm NIR light group (***$p < 0.001$) (Figure 6b), with tumor weights one-third that of untreated mice (Figure 6c).

Throughout the treatment, minor fluctuations were observed in the weight of mice in each group (Figure 6d). Moreover, hematoxylin and eosin (H&E) (Figure 6f) and terminal deoxynucleotidyl transferase dUTP nick end labeling (TUNEL) (Figure 6g) staining of the 4T1 tumor tissue following **Ru2** and 700 nm LED light treatment revealed extensive areas of apoptosis and necrosis, while no significant damage was observed for **Ru2** or 700 nm LED light alone. To evaluate the effect of light penetration on cell death in vivo, 465 nm LED light excited **Ru1** and 700 nm LED light excited **Ru2** were separately *i.t.* injected into the tumor tissue of 4T1 subcutaneous tumor bearing mice. 24 h after irradiated by 99.6 J cm$^{-2}$ 465 nm or 700 nm LED light, tumor tissue were collected for vertical slice from epidermal to deep tissue and H&E staining analysis. From pathological sections, **Ru2** injected tumor tissue larger range of damaged 4T1 cells was found in **Ru2** injected tumor tissue than **Ru1** injected tumor tissue. This result suggested 700 nm LED light excited **Ru2**-based anticancer therapy showed enhanced deep tissue therapeutic ability, compared with 465 nm LED light excited **Ru1**-based anticancer therapy (Figure S32, Supporting Information). Most importantly, examination of main organs slices collected from mice 1 or 7 d following the intravenous injection of **Ru2** showed no evident signs of destructive cell necrosis or inflammation lesions in the major organs (Figure 6h). Thus, **Ru2** exhibits low biological toxicity but photoexcited anticancer therapeutic effect toward 4T1 cancer cells both in vitro and in vivo.

## 3. Conclusion

In this study, we designed and synthesized a novel one photon NIR light-triggered Ru(II) PACT complex **Ru2**, to address the challenges including light absorption limitation of photoactivated metallic complex and investigate the intracellular anticancer mechanism of action. It is found that incorporating a D–A–D linker shifted the absorbance of Ru(II) complexes into the NIR region (reaching 800 nm), a big advance for the study of photoactivated Ru(II) complexes.

Moreover, the intramolecular charge transition from the D–A–D linker and the intraligand charge transfer transition populated the triplet excited state and avoided the activation of metal-center state. Upon 700 NIR light activation, **Ru2** exhibited typical type I photosensitization ability and catalyzed oxidation of coenzyme NADPH, which destroyed the intracellular antioxidative system of cancer cells. As a result, **Ru2** exhibited strong photoactivated cytotoxicity against diverse cancer cell lines in vitro under normoxia and hypoxia, as well as 4T1 tumor in vivo upon exposure to 700 nm light Anticancer mechanism studies investigated that **Ru2** induced intracellular redox imbalance, ER stress and cytoplasmic calcium overload, leading to the irreversible death of cancer cells. This study highlights the potential of **Ru2**, a NIR light activated Ru(II) complex, for phototherapeutic application.

## 4. Experimental Section

*Materials*: All reagents and materials from commercial sources. $RuCl_3 \cdot xH_2O$ and methylene blue trihydrate were purchased from Macklin. 2,2′-Bipyridine was purchased from Sigma-Aldrich. Tetrakis(triphenylphosphine)palladium,5-bromo-2,2′-bipyridine, 2,9-dimethyl-1,10-phenanthroline, $K_2CO_3$, $LiCl_3$ cis-platin, ammonium hexafluorophosphate, chlorin e6 (Ce6), Dihydrorhodamine 123 (DHR123), Reactive Oxygen Species Assay Kit (ROS Assay Kit), dihydronicotinamide adenine dinucleotide phosphate tetrasodium salt (NADPH) were purchased from Bidepharm. Tetrabutylammonium hexafluorophosphate was purchased from Aladdin. 2,5-bis(2-ethylhexyl)−3,6-bis(5-(trimethylstannyl)thiophen-2-yl)−2,5-dihydropyrrolo[3,4-c]pyrrole-1,4-dione was purchased by Derthon. OxiVision Green hydrogen peroxide sensor was purchased by AAT Bioquest. Mouse breast cancer cell line (4T1), human breast cancer cell line (MCF-7), human lung carcinoma cell line (A549), and DDP-resistant human lung adenocarcinoma cell line (A549/DDP) were obtained from Procell Life Science&Technology Co.,Ltd. Dulbecco Modified Eagle Medium (DMEM), fetal bovine serum (FBS), penicillin/streptomycin, and phosphate buffered saline (PBS) were bought from Gibco. BIP, CHOP, Casepase-12-specific antibodies were purchased from Proteintech. Mito Tracker Green FM, Lyso Tracker Green DND-26 and MitoSOX Red mitochondrial superoxide indicator were purchased from Life Technologies Corporation. Mitochondrial membrane potential assay kit with JC-1, Annexin V-FITC/PI Apoptosis Detection Kit, ER-Tracker Green, Hoechst 33 342, Tubulin-Tracker Green Staining Kit, Fluo-4 AM (Calcium ion fluorescent probe), and Dihydroethidium (DHE) and ATP Assay Kit were purchased from Beyotime Biotechnology. GSH-Glo Glutathione Assay, NADP/NADPH-Glo Assay product was purchased from Promega.

*Instruments*: $^1$H NMR spectra were recorded on Bruker Advance III. $^1$H-$^1$H COSY and $^{13}$C NMR spectra were recorded on Bruker AVANCE III 500 MHz spectrometer. Positive ion high resolution mass spectra were obtained by LCMS-IT-TOF (Shimadzu, Japan). UV–vis absorption spectra were recorded on a double beam UV-vis spectrophotometer (YOUKE, T3202S). The fluorescence spectra and emission quantum yield measurements were measured on a Techcomp FL970 fluorescence spectrophotometer. The low-temperature fluorescence spectra were detected by combined photoluminescence lifetime and steady state spectrometer (FLS1000, Edinburgh Instruments Ltd). Confocal microscopy was done with a laser confocal microscopy (LEICA-SP5II, LCSM 880, Carl Zeiss, Göttingen, Germany). The nanosecond transient absorption spectra were measured on a laser flash photolysis spectrometer (LP980, Edinburgh Instruments, Ltd., U.K.).

*Synthesis and Characterization*: Synthesis of $Ru(dmp)_2Cl_2$: To a mixture of 2,9-dimethyl-1,10-phenanthroline(dmp) (1.25 g, 6 mmol), $RuCl_3 \bullet xH_2O$ (0.62 g, 3 mmol), and $LiCl_3$ (0.38 g, 8.9 mmol) were added to 20 mL of *N*,*N*-dimethylformamide in a two neck flask. The mixture was degassed with $N_2$ for 20 min, and was then refluxed for 8 h. After cooling to room temperature, an appropriate amount of acetone was added, and it was placed in the refrigerator overnight. The black precipitate was collected by vacuum filtration. The black solid was washed with cold water and acetone. Yield: 0.43 g (24.3%).

*Synthesis of [Ru(2,9-dmp)2(bpγ)](PF6)2 (Ru1)*: **Ru1** was prepared following reported literature.[22]

*Synthesis of Ru-3T(PF6)2*: **Ru-3T** was prepared following reported literature.[15]

*Synthesis of Ru2*: $Ru(2,9\text{-}dmp)_2Cl_2$ (0.177 g, 0.3 mmol) and 5-bromo-2,2′-bipyridine (bpy-Br) (0.071 g, 0.3 mmol) were mixed in ethylene glycol (10 mL), stired and heated at 80 °C overnight. Then the mixture was cooled to room temperature, followed by addition of saturated aqueous solution of $NH_4PF_6$. The crude product of $[Ru(2,9\text{-}dmp)_2(bpy\text{-}Br)](PF_6)_2$ was collected by filtration and washed by water. Combine $[Ru(2,9\text{-}dmp)_2(bpy\text{-}Br)](PF_6)_2$ (0.15 g,0.14 mmol), $Pd(PPh_3)_4$ (3mol%) and 2,5-bis(2-ethylhexyl)−3,6-bis(5-(trimethylstannyl)thiophen-2-yl)−2,5-dihydropyrrolo[3,4-c]pyrrole-1,4-dione (0.051 g, 0.07 mmol) in a mixture of degassed toluene (6 mL) and DMF(6 mL). Heat the mixture at 115 °C for 20 h under $N_2$. Allow the solution to cool to room temperature. The saturated NaCl aqueous solution was added, and the crude product of **Ru2** was collected by filtration, purified by neutral alumina column chromatography (eluent:dichloromethane/acetonitrile = 3/1). HR-ESI-MS (MeOH): $[M\text{-}2PF_6]^{2+}$ calcd for $[C_{106}H_{100}N_{14}O_2Ru_2S_2]^{4+}$: 467.1425, found $[M\text{-}2PF_6]^{2+}$: 467.1435. $^1$H NMR (500 MHz, DMSO-$d_6$) $\delta$ 9.04 – 8.99 (m, 2H), 8.90 (d, 2H), 8.61 (s, 1H), 8.59 (dd, 4H), 8.54 (dd,4H), 8.47 (d, 2H), 8.42 (d,2H), 8.37 (d, 2H), 8.28 (d, 2H), 8.25 (d, 2H), 8.05 – 7.98 (m, 3H), 7.98 – 7.96 (m, 2H), 7.96 (s, 1H), 7.66 – 7.61 (m, 4H), 7.41 – 7.34 (m, 2H), 7.28 (d,2H), 7.15 (dd, J = 12.2, 4.6 Hz, 4H), 4.02 (d, 4H), 2.05 (s, 6H), 1.97 – 1.86 (m, 20H), 1.63 (s, 2H), 1.32 – 1.13 (m, 16H), 0.87 (t, 5H), 0.77 – 0.73 (m, 5H).

*High Performance Liquid Chromatography (HPLC) Analysis*: **Ru2** HPLC analysis was performed on a Waters alliance e2695. The complexes were analyzed by reversed-phase Agilent ZORBAX SB-C18 column (4.6 × 250 mm) at 25 °C with a flow rate of 1 mL $min^{-1}$ and UV-detector was set at full absorption band. The solvent system consists of two eluents: mobile phase A was water /formic acid (1000/1, v/v) while mobile phase B was acetonitrile/formic acid (1000/1, v/v). The procedure run with a isocratic: 0.01 min (5% phase B), 5 min (5% phase B), a gradient: 10 min (5% phase B), 15 min (100% phase B). All HPLC analysis were analyzed using the same method.

*UV–vis Absorption Spectra*: The UV–vis spectra of the complexes were recorded by a double beam UV–vis spectrophotometer (YOUKE, T3202S) with 1 cm path-length quartz cuvettes, and the obtained data was processed using Origin software. The UV–visible spectra absorption measurement of **Ru1** and **Ru2** ($10 \times 10^{-6}$ M) experiments were carried out at 298 K from 800 to 300 nm.

*Phosphorescence Spectra*: Phosphorescence emission measurements were performed on a Techcomp FL970 fluorescence spectrophotometer. The complexes of **Ru2** ($10 \times 10^{-6}$ M) in eight different solvents were excited at $\lambda_{ex}$ = 635 nm and in a 1-cm quartz cuvette at 298 K. The hypoxia photoluminescence spectra of **Ru2** ($10 \times 10^{-6}$ M) in dichloromethane (DCM) were obtained after purging Ar into the solution for 30 min before excited at 635 nm. The incident slit and exit slit were set as 10 nm.

*Photoluminescence Quantum Yield*: Photoluminescence spectra were obtained with a fluorescence spectrophotometer. The relative photolumi-

nescence quantum yields were determined with MB as the standard using the following equation

$$F_x = \Phi_s \times (F_x/F_s) \times (A_s/A_x) \times (n_x/n_s) \quad (1)$$

where Φ represents quantum yield; *F* stands for integrated area under the corrected emission spectrum; *A* is absorbance at 635 nm, the excitation wavelength; *n* is the refractive index of the solution; and the subscripts x and s refer to the complex sample and the standard, respectively. **Ru2** were diluted from a stock solution in DMSO to achieve an absorbance = 0.1 at 635 nm in acetonitrile. The $\Phi_p$ value for MB in acetonitrile at 298 K were measured to be 0.01 and 0.08 respectively. These values for the phosphorescence quantum yield of MB have been reported in previous literatures.[23]

*Temperature Dependent Photoluminescence Spectra*: The **Ru2** (dissolved in a solution of V ethanol: V methanol = 4:1) was quickly cooled by immersing the sample into liquid nitrogen to freeze the molecules in their original environment. The fluorescence emission spectra were then acquired on a combined photoluminescence lifetime and steady state spectrometer (FLS1000, Edinburgh Instruments Ltd) with a cryostat (TeslatronPT, Oxford Instruments) as the temperature was gradually raised within about 1–2 h.

*Nanosecond Transient Absorption Spectra*: The nanosecond transient absorption spectra and triplet excited-state lifetime were recorded on LP980 laser flash photolysis spectrometer (Edinburg Instruments, Ltd., UK). All samples ($10 \times 10^{-6}$ M) were dissolved in DCM and deaerated with Ar for ≈15 min before measurement, then excited with a nanosecond pulsed laser (Opolette 355II+UV nanosecond pulsed laser. OPOTEK) at 600 nm (5 mJ per pulse). The data of kinetic decay trace and curve fitting were analyzed with L900 software.

*Computational Details*: All the optimizations were performed with the Gaussian 09 software package. The ground state geometry optimizations and spin density isosurfaces of the complexes were calculated by using density functional theory (DFT) method with the optimized ground state and triplet state geometries, respectively. The energy levels and orbitals of the singlet and triplet excited states calculations were performed by using time-dependent density functional theory (TD-DFT) method. All structures were optimized at the B3LYP/6-31G* level of DFT with an SDD basis set to describe Ru atoms. Frequency calculations were performed to confirm the characteristics of all the calculated structures as minima.

*Photoactivation Properties Study*: Photoactivation properties were analyzed by HPLC and UV–vis absorption spectra. For the UV–vis absorption spectra, **Ru2** ($10 \times 10^{-6}$ M) were dissolved in PBS with irradiation at 700 nm at the different intervals and recorded UV–vis absorption spectra (700 nm, 285 J $cm^{-2}$). For the HPLC analysis, **Ru2** ($10 \times 10^{-6}$ M) were dissolved in $CH_3OH$ with irradiation at 700 nm at the same intervals and recorded HPLC spectra (700 nm, 285 J $cm^{-2}$). The calculation of photosubstitution quantum yield ($\Phi_{ps}$) is referred to the previous report.[15]

*Photocatalytic Reactions of RuII Complexes with NADPH*: Reactions between **Ru2** ($5 \times 10^{-6}$ M) and NADPH in PBS at different ratios were monitored by UV–vis spectroscopy at 298 K in the dark or on irradiation with 700 nm (57 J $cm^{-2}$) light. The concentration NADH and NADPH was obtained by using the extinction coefficient $\epsilon_{339} = 6300\ M^{-1}\ cm^{-1}$. The turnover number of catalysis was calculated using the following equations

$$\left[NADP^+\right] = [Abs(339\ nm)_{initial} - Abs(339\ nm)_{final}]/Abs(339\ nm)_{initial} \times [NADPH] \quad (2)$$

$$\text{Turnovernumber (TON)} = [NADP+] / [Catalyst] \quad (3)$$

$$\text{Turnoverfrequency (TOF)} = \text{Turnovernumber/time (h)} \quad (4)$$

*Detection of $H_2O_2$ Generation*: For the reaction of complexes **Ru2** ($10 \times 10^{-6}$ M) with amino acids (10 mg $mL^{-1}$), adenosines (10 mg $mL^{-1}$), ctDNA (10 mg $mL^{-1}$), human serum albumin (HSA) (10 mg $mL^{-1}$), and a variety of coenzymes (10 mg $mL^{-1}$) in the PBS solution at 298 K in the dark or after irradiation for 20 min (700 nm, 57 J $cm^{-2}$), $H_2O_2$ was detected by OxiVision Green hydrogen peroxide sensor (AAT Bioquest). The $H_2O_2$ generation level of the solution could be recorded by the Tecan/Infinite E plex.

*Determination of Singlet Oxygen Generation*: The production of singlet oxygen ($^1O_2$) in solution was detected using 9, 10-anthracenediyl bis(methylene) dimalonic acid (ABDA) as $^1O_2$ probe. **Ru2** ($5 \times 10^{-6}$ M) in PBS was mixed with ABDA ($200 \times 10^{-6}$ M). The reaction mixture was taken in a quartz cuvette and the absorbance of ABDA was monitored by UV-vis at 298 K after 700 nm (7.1 J $cm^{-2}$) light irradiation for different interval.

*Determination of Superoxide Anion ($O_2^{\bullet-}$)*: The production of superoxide anion ($O_2^{\bullet-}$) in solution was detected using Dihydrorhodamine 123 (DHR123) as $O_2^{\bullet-}$ probe. **Ru2** ($5 \times 10^{-6}$ M) in PBS was mixed with DHR123 ($10 \times 10^{-6}$ M). The reaction mixture was taken in a quartz cuvette and the fluorescence of DHR123 was monitored by Techcomp FL970 fluorescence spectrophotometer at 298 K after 700 nm (7.1 J $cm^{-2}$) light irradiation for different interval.

*Determination of Hydroxyl Radical (OH•) Generation*: The production of hydroxyl radical (OH•) in solution was detected using hydroxyphenyl fluorescein (HPF) as probe. **Ru2** ($5 \times 10^{-6}$) in PBS was mixed with HPF ($5 \times 10^{-6}$ M). The reaction mixture was taken in a quartz cuvette and the fluorescence of HPF was monitored by Techcomp FL970 fluorescence spectrophotometer at 298 K after 700 nm (14.3 J $cm^{-2}$) light irradiation for different interval.

*Cell Culture*: Cell lines A549, A549/DDP, 4T1, MCF-7 were maintained in DMEM medium supplemented with 10% fetal bovine serum, and 1% penicillin–streptomycin solution. All cells were grown at 310 K in a humidified incubator which provided an atmosphere of 5% $CO_2$.

*Cell Proliferation Inhibition Assay*: Cell viability was determined by resazurin assay and performed in triplicate in 96-well plates. Cells were maintained in DMEM with 10% FBS and 1% penicillin–streptomycin solution. 100 µL warm culture medium containing about $5 \times 10^3$ cells were seeded per well in 96-well plates, and placed in a 37 °C, 5% $CO_2$ incubator for 24 h to achieve cell attachment. After that, the medium was removed completely, the fresh medium containing different concentrations of the compounds was added to each well. The final concentration of DMSO was lower than 0.1% v/v. After incubation for 6 h, without changing medium, the dark groups were placed in the incubator for further incubation, the light groups were irradiated with 700 nm light (99.6 J $cm^{-2}$) followed by 42 h incubation. After that, the medium was removed, resazurin solution (80 µL, 100 mg $mL^{-1}$) was added to each well and incubated for another 4 h at 37 °C. Then the fluorescence intensity at $E_x/E_m$ 540/590 was measured with a microplate reader (Tecan/Infinite E plex).

The operation procedure under hypoxic conditions was consistent with that of normoxia. The well plates were only transferred to 1% $O_2$ work station after cell attachment, and all subsequent operations were carried out in the work station.

*Colocalization Assays*: **Ru2** colocalization assays 4T1 cells were seeded in a confocal dish and cultured under favorable conditions. After 48 h, **Ru2** ($20 \times 10^{-6}$ M) was added to incubate with the cells for 4 h and were further stained with ER, Lyso-, and Mito-Tracker ($100 \times 10^{-9}$ M) for 30 min. Intracellular distribution was done by confocal microscope (LCSM 880, Carl Zeiss, Göttingen, Germany) with a 63× objective lens. **Ru2** was excited at 633 nm, Lyso- and Mito- Tracker were excited at 488 nm. The phosphorescence/fluorescence was collected at 700 ± 50 nm for **Ru2** and 550 ± 50 nm for ER, Lyso- and Mito-Tracker.

ROS colocalization assays 4T1 cells were seeded in a confocal dish and cultured under favorable conditions. After 48 h, **Ru2** ($0.1 \times 10^{-6}$ M) was added to incubate with the cells for 2 h and were then irradiated with red light (700 nm, 99.6 J $cm^{-2}$). Further cells were stained with ER, Lyso- and Mito-Tracker ($100 \times 10^{-9}$ M) for 30 min. Intracellular distribution was done by fluorescence microscope (BZ-X800, KEYENCE) with a 40× objective lens.

*Detection of Intracellular NADPH, GSH, and ATP Level*: 4T1 cells were seeded per well in 6-well plates in incubator for 24 h. Then the cells were

treated with different concentration of **Ru2** for 2 h. For light treatment, the cells were then irradiated with red light (700 nm, 99.6 J $cm^{-2}$) and further were incubated for 1 h. The $NADP^+$/NADPH Assay Kit (Beyotime), GSH-Glo Glutathione Assay Kit, and ATP Assay Kit (Beyotime) were used to measure the intracellular NADPH, GSH, and ATP level. The absorbance or luminescence was recorded using a microplate reader. Three replicates were set for each sample, and the standard deviations were calculated in each group.

*Microtubule Polymerization Inhibition*: To evaluate the potency of inhibition of microtubule by **Ru2** in 4T1 cells, tubulins were stained using Tubulin-Tracker Green Staining Kit (Beyotime). The cells were seeded on a confocal dish. After that, cells were incubated with **Ru2** ($0.1 \times 10^{-6}$ M) at 310 K for 2 h. The light groups then were on irradiation at 635 nm (99.6 J $cm^{-2}$) light. Furthermore, cells were incubated in the dark at 310 K, 5% $CO_2$ incubator for another 4 h. Afterward, the cells were treated by Tubulin-Tracker Green for 1 h with light protection. Then cells were washed with PBS 3 times, Hoechst 33 342 was then added for nuclear staining. All the samples were imaged and analyzed by confocal laser scanning microscope (LEICA-SP5II). Blue fluorescence (Hoechst 33 342, $\lambda_{ex} = 405$ nm, $\lambda_{em} = 450 \pm 30$ nm); green fluorescence (Tubulin-Tracker Green, $\lambda_{ex} = 488$ nm, $\lambda_{em} = 540 \pm 30$ nm.)

*Measurements of Intracellular Calcium Ion*: 4T1 cells were seeded into 6-well plate at the density of 200 000 cells per well and incubated for 48 h. After that, cells were incubated with **Ru2** ($0.1 \times 10^{-6}$ M) at 310 K for 2 h. The light groups then were on irradiation at 635 nm (99.6 J $cm^{-2}$) light and were incubated for 1 h. The intracellular calcium ion levels were measured with the diluted Fluo-4 AM ester stock solution (Beyotime, China) ($3 \times 10^{-6}$ M with PBS). The Fluo-4 AM ester solution was added and incubated with BMSCs for 30 min at 37 °C. Then, after removing the Fluo-4 AM ester solution, the cells were rinsed by PBS for three times. A part of cells was resuspended with PBS, the fluorescence intensity was measured with flow cytometer (Beckman, CytoFLEX) at the excitation wavelength of 488 nm. Meanwhile, the other part of cell's fluorescent images are captured by an inverted fluorescence microscope.

*BIP, CHOP, and Casepase-12 Analysis*: 4T1 cells were seeded in 6-well plates at a density of $4 \times 10^5$ per well. After 24 h, Then the cells were treated with **Ru2** ($0.1 \times 10^{-6}$ M) for 2 h. For light treatment, the cells were then irradiated with red light (700 nm, 99.6 J $cm^{-2}$) and further were incubated for 1 h. All cells were collected, the expression of BIP, CHOP, and Casepase-12 upon formulation treatment was analyzed by western blotting. The cell lysates containing identical protein (40 µg) were subjected to standard electrophoresis, followed by antibody incubation at 4 °C. The dilution ratio for the first antibody was 1:1000. Regarding the secondary antibody, the dilution ratio was 1:5000. The protein bands were developed via the ECLTM western blotting detection reagents. SuperSignal West Pico Chemiluminescent Substrate chemiluminescent reagent was used, the film was pressed with X-ray film, developed with developer and fixer.

*Determination of Intracellular Reactive Oxygen Species*: 4T1 cells were seeded into 96-well plate at the density of 5000 cells per well and incubated for 48 h. After that, cells were incubated with **Ru2** ($0.5/1.0 \times 10^{-6}$ M) at 310 K for 2 h. The light groups then were on irradiation at 700 nm (99.6 J $cm^{-2}$) light. Further, cells were incubated with $10 \times 10^{-6}$ M Reactive Oxygen Species Assay Kit (DCFH-DA) at 310 K for 30 min in the dark and washed once with PBS before observed by an inverted fluorescence microscope. The fluorescence intensity was also measured by flow cytometry under the same treatment conditions.

*Determination of Intracellular Superoxide Anion ($O2^{-\bullet}$) and Hydroxyl Radical ($OH^{\bullet}$)*: 4T1 cells were seeded into 96-well plate at the density of 5000 cells per well and incubated for 48 h. After that, cells were incubated with **Ru2** ($0.5/1.0 \times 10^{-6}$ M) at 310 K for 2 h. The light groups then were on irradiation at 700 nm (99.6 J $cm^{-2}$) light. Further, cells were incubated with $5 \times 10^{-6}$ M dihydroethidium (DHE) and hydroxyphenyl fluorescein (HPF) at 310 K for 30 min in the dark and washed once with PBS before observed by an inverted fluorescence microscope.

*Mitochondrial Membrane Potentials ($\Delta\Psi m$) Assays*: The mitochondrial membrane potential was determined by JC-1 dye. 4T1 cells were seeded into 96-well plate at the density of 5000 cells per well and incubated for 48 h. After that, cells were incubated with **Ru2** at 310 K for 2 h. The light groups then were on irradiation at 700 nm (99.6 J $cm^{-2}$) light. Furthermore, cells were incubated in the dark at 310 K, 5% $CO_2$ incubator for another 1 h. Subsequently, cells were stained with JC-1 (2.5 µg $mL^{-1}$) at 310 K for 20 min in the dark and washed once with PBS. The cells were imaged by an inverted fluorescence microscope.

*Detection of Intracellular Mitochondrial Superoxide*: 4T1 cells were seeded into 96-well plate at the density of 5000 cells per well and incubated for 48 h. After that, cells were incubated with **Ru2** ($0.1 \times 10^{-6}$ M) at 310 K for 2 h. The light groups then were on irradiation at 635 nm (99.6 J $cm^{-2}$) light. Furthermore, cells were incubated in the dark at 310 K, 5% $CO_2$ incubator for another 1 h. Afterward, cells were incubated with $5 \times 10^{-6}$ M MitoSOX red probe at 310 K for 10 min in the dark and washed twice with PBS before observed by an inverted fluorescence microscope.

*Annexin V-FITC/PI Assays*: Mode of cell death was detected by Annexin V-FITC/PI dual staining. 4T1 cells were seeded into 96-well plate at the density of 5000 cells per well and incubated for 48 h. After that, cells were incubated with **Ru2** ($0.05/0.1 \times 10^{-6}$ M) at 310 K for 2 h. The light groups then were on irradiation at 700 nm (99.6 J $cm^{-2}$) light and further were incubated for 1 h. After that, Cells were stained with annexin V-FITC (2.5 µL) and PI (5 µL) stock solution in the dark for 15 min at ambient temperature. The fluorescence images were obtained within an hour on an inverted fluorescence microscope. The fluorescence intensity was also measured by flow cytometry under the same treatment conditions

*Tumor Model*: Female Balb/c nude mice were purchased from Beijing Vital River Laboratory Animal Biotechnology Co. Ltd, and all animal experiments were carried out under the permission by Wenzhou Medical University Laboratory Animal Resources Center (no. xmsq 2023-0282). One million 4T1 cancer cells in 25 µL PBS were subcutaneously injected to the right back of each mouse. 6 d after injection, the mice, whose tumor volumes reached about 80 $mm^3$, were selected for further experiments.

*In Vivo PDT*: The NIR light activated in vitro phototoxicity of **Ru2** inspired us to investigate the in vivo anticancer profile of **Ru2** against the 4T1 tumor-bearing mice. Seven days after 4T1 cells were injected into mice, the mice were randomly distributed into four groups ($n = 5$): (1) Untreated; (2) **Ru2** alone (i.t. injection 30 µg); (3) light alone (700 nm, 99.6 J $cm^{-2}$); (4) **Ru2** + light (i.t. injection 6 µg; 700 nm, 99.6 J $cm^{-2}$). Mice in group one were anesthetized with 1% pentobarbital sodium solution and then intratumorally injected with 25 µL of PBS containing 30% DMSO without further treatment. For mice in group two, 25 µL of PBS containing 30% DMSO and 30 µg **Ru2** were intratumorally injected after anesthetized. Mice in group three were anesthetized and intratumorally injected with 25 µL of PBS containing 30% DMSO. 30 min after injection mice were irradiated by the 700 nm light. Mice in group four were anesthetized and intratumorally injected with 25 µL of PBS containing 30% DMSO and 6 µg **Ru2**. 30 min after injection mice were irradiated by the 700 nm light. Tumor sizes were monitored every two days for 14 d or tumor volume over 1000 $mm^3$. The tumor volumes were calculated by the formula: volume = 0.5×length×$width^2$. For histology diagnosis, at 24 h after treatment, tumor tissues were collected from different groups mice. The tumor tissue was fixed with 10% formalin, then embedded in paraffin, and then sectioned and stained with H&E and TUNEL.

*Maximum Tolerable Dose (MTD)*: Balb/c mice were purchased from Beijing Vital River Laboratory Animal Biotechnology Co. Ltd, and all animal experiments were carried out under the permission by Laboratory Animal Center, Wenzhou Medical University Laboratory Animal Resources Center. Balb/c mice (6 weeks, average weight ≈20 g) were randomly divided into several groups ($n = 6$ per group) for **Ru2** treatments: 3, 6, 12, 18, and 24 mg $kg^{-1}$. The solution including **Ru2** dissolved in 0.4 mL PBS containing 30% DMSO was used for single caudal vein injection per mice.

*Statistical Analysis*: All experiments were performed at least three times. All data in this work are presented as mean ± standard deviation (SD). Ordinary one-way ANOVA was used for multiple comparisons. A two-tailed *t*-test was used for two-group comparisons. Statistical significance was set at $^{***}p < 0.001$, $^{**}p < 0.01$, or $^{*}p < 0.05$.

## Supporting Information

Supporting Information is available from the Wiley Online Library or from the author.

## Acknowledgements

A.D. and S.C. contributed equally to this work. The authors appreciate the financial support from the National Natural Science Foundation of China (NSFC 22277153, 22007104, 21931002, 22077085), Guangdong Basic and Applied Basic Research Foundation (2021B1515020050, 2023B1515020060), the Science and Technology Foundation of Shenzhen (JCYJ20210324095200002, JCYJ20220531103405012, RCYX20221008092906021), the Fundamental Research Funds for the Central Universities (22lgqb37).

[Correction added on 18 May 2024 after first online publication: Acknowledgment section is updated in this version.]

## Conflict of Interest

The authors declare no conflict of interest.

## Data Availability Statement

The data that support the findings of this study are available in the supplementary material of this article.

## Keywords

donor–acceptor–donor (D–A–D) linker, NIR, photoactivated therapy, redox imbalance, Ru(II) complex

Received: March 13, 2024
Revised: April 12, 2024
Published online:

[1] a) K. D. Miller, A. P. Ortiz, P. S. Pinheiro, P. Bandi, A. Minihan, H. E. Fuchs, D. M. Tyson, G. Tortolero-Luna, S. A. Fedewa, A. M. Jemal, R. L. Siegel, *Ca-Cancer J. Clin.* **2021**, *71*, 466; b) R. L. Siegel, K. D. Miller, N. S. Wagle, A. Jemal, *Ca-Cancer J. Clin.* **2023**, *73*, 17.

[2] a) X. Jing, F. Yang, C. Shao, K. Wei, M. Xie, H. Shen, Y. Shu, *Mol. Cancer.* **2019**, *18*, 157; b) Y. Hayashi, A. Yokota, H. Harada, G. Huang, *Cancer Sci.* **2019**, *110*, 1510.

[3] S. Y. Tam, V. W. C. Wu, H. K. W. Law, *Front. Oncol.* **2020**, *10*, 486.

[4] R. Kumari, D. Sunil, R. S. Ningthoujam, *J. Controlled Release.* **2020**, *319*, 135.

[5] a) B. S. Howerton, D. K. Heidary, E. C. Glazer, *J. Am. Chem. Soc.* **2012**, *134*, 8324; b) H. D. Cole, J. A. Roque 3rd, G. Shi, L. M. Lifshits, E. Ramasamy, P. C. Barrett, R. O. Hodges, C. G. Cameron, S. A. McFarland, *J. Am. Chem. Soc.* **2022**, *144*, 9543; c) Y. Huang, Y. Zhou, X. Zeng, D. Zhang, S. Wu, *Adv. Mater.* **2023**, *35*, 2305517; d) J. Karges, T. Yempala, M. Tharaud, D. Gibson, G. Gasser, *Angew. Chem., Int. Ed.* **2020**, *59*, 7069; e) L. Zhang, P. Wang, X. Zhou, L. Bretin, X. Zeng, Y. Husiev, E. A. Polanco, G. Zhao, L. S. Wijaya, T. Biver, S. Le Devedec, W. Sun, S. Bonnet, *J. Am. Chem. Soc.* **2023**, *145*, 14963; f) X. Zeng, Y. Wang, J. Han, W. Sun, H. J. Butt, X. Liang, S. Wu, *Adv. Mater.* **2020**, *32*, 2003294; g) Z. Deng, H. Li, S. Chen, N. Wang, G. Liu, D. Liu, W. Ou, F. Xu, X. Wang, D. Lei, P. Lo, Y. Li, J. Lu, M. Yang, M. He, G. Zhu, *Nat. Chem.* **2023**, *15*, 930; h) P. K. L. Fu, S. Abuzakhm, C. Turro, *Photochem. Photobiol.* **2005**, *81*, 89; i) Q. Chen, J. A. Cuello-Garibo, L. Bretin, L. Zhang, V. Ramu, Y. Aydar, Y. Batsiun, S. Bronkhorst, Y. Husiev, N. Beztsinna, L. Chen, X. Zhou, C. Schmidt, I. Ott, M. J. Jager, A. M. Brouwer, B. E. Snaar-Jagalska, S. Bonnet, *Chem. Sci.* **2022**, *13*, 6899; j) F. Bisceglie, G. Pelosi, N. Orsoni, M. Pioli, M. Carcelli, P. Pelagatti, S. Pinelli, P. J. Sadler, *Int. J. Mol. Sci.* **2022**, *23*, 7624; k) M. Salierno, E. Marceca, D. S. Peterka, R. Yuste, R. Etchenique, *J. Inorg.* **2010**, *104*, 418; l) N. P. Toupin, S. J. Steinke, M. K. Herroon, I. Podgorski, C. Turro, J. J. Kodanko, *Photochem. Photobiol.* **2022**, *98*, 378. m) K. Arora, M. Herroon, M. H. Al-Afyouni, N. P. Toupin, T. N. Rohrabaugh, L. M. Loftus, I. Podgorski, C. Turro, J. J. Kodanko, *J. Am. Chem. Soc.* **2018**, *140*, 14367; n) N. Toupin, S. J. Steinke, S. Nadella, A. Li, T. N. Rohrabaugh, E. R. Samuels, C. Turro, I. F. Sevrioukova, J. J. Kodanko, *J. Am. Chem. Soc.* **2021**, *143*, 9191. o) M. H. Al-Afyouni, T. N. Rohrabaugh, K. F. Al-Afyouni, C. Turro, *Chem. Sci.* **2018**, *9*, 6711.

[6] a) C. Imberti, P. Zhang, H. Huang, P. J. Sadler, *Angew. Chem., Int. Ed.* **2020**, *59*, 61; b) L. Gourdon, K. Cariou, G. Gasser, *Chem. Soc. Rev.* **2022**, *51*, 1167; c) C. Mari, V. Pierroz, S. Ferrari, G. Gasser, *Chem. Sci.* **2015**, *6*, 2660.

[7] a) Y. Luo, B. Cao, M. Zhong, M. Liu, X. Xiong, T. Zou, *Angew. Chem., Int. Ed.* **2022**, *61*, 202116068; b) A. Zamora, G. Vigueras, V. Rodriguez, M. D. Santana, J. Ruiz, *Coord. Chem. Rev.* **2018**, *360*, 34; c) J. Liu, A. W. Prentice, G. J. Clarkson, J. M. Woolley, V. G. Stavros, M. J. Paterson, P. J. Sadler, *Adv. Mater.* **2023**, *35*, 2210363.

[8] E. P. V. Geest, S. K. Götzfried, D. M. Klein, N. Salitra, S. Popal, Y. Husiev, C. J. V. d. Griend, X. Zhou, M. A. Siegler, G. F. Schneider, S. Bonnet, *Photochem. Photobiol.* **2023**, *99*, 777.

[9] a) Z. Fan, Y. Rong, T. Sadhukhan, S. Liang, W. Li, Z. Yuan, Z. Zhu, S. Guo, S. Ji, J. Wang, R. Kushwaha, S. Banerjee, K. Raghavachari, H. Huang, *Angew. Chem., Int. Ed.* **2022**, *61*, 202202098; b) S. Wei, H. Liang, A. Dao, Y. Xie, F. Cao, Q. Ren, A. Yadav, R. Kushwaha, A. A. Mandal, S. Banerjee, P. Zhang, S. Ji, H. Huang, *Sci. China: Chem.* **2023**, *66*, 1482; c) X. Da, Z. Wang, Y. Jian, C. Zhang, Y. Hou, Y. Yao, X. Wang, Q. Zhou, *Inorg. Chem. Front.* **2022**, *9*, 254.

[10] a) L. Zeng, P. Gupta, Y. Chen, E. Wang, L. Ji, H. Chao, Z. Chen, *Chem. Soc. Rev.* **2017**, *46*, 5771; b) F. E. Poynton, S. A. Bright, S. Blasco, D. C. Williams, J. M. Kelly, T. Gunnlaugsson, *Chem. Soc. Rev.* **2017**, *46*, 7706; c) S. Chakrabortty, B. K. Agrawalla, A. Stumper, N. M. Veg, S. Fischer, C. Reichardt, M. Kögler, B. Dietzek, M. Feuring-Buske, C. Buske, S. Rau, T. Weil, *J. Am. Chem. Soc.* **2017**, *139*, 2512; d) H. Huang, B. Yu, P. Zhang, J. Huang, Y. Chen, G. Gasser, L. Ji, H. Chao, *Angew. Chem., Int. Ed.* **2015**, *54*, 14049.

[11] a) R. Boerhan, W. Sun, N. Tian, Y. Wang, J. Lu, C. Li, X. Cheng, X. Wang, Q. Zhou, *Dalton Trans.* **2019**, *48*, 12177; b) L. N. Lameijer, T. G. Breve, V. H. S. van Rixel, S. H. C. Askes, M. A. Siegler, S. Bonnet, *Chemistry.* **2018**, *24*, 2709; c) A. Busemann, I. Flaspohler, X. Zhou, C. Schmidt, S. K. Goetzfried, V. H. S. van Rixel, I. Ott, M. A. Siegler, S. Bonnet, *J. Biol. Inorg. Chem.* **2021**, *26*, 667; d) J. A. Cuello-Garibo, E. Perez-Gallent, L. van der Boon, M. A. Siegler, S. Bonnet, *Inorg. Chem.* **2017**, *56*, 4818.

[12] a) C. E. McCusker, D. Hablot, R. Ziessel, F. N. Castellano, *Inorg. Chem.* **2012**, *51*, 7957; b) W. Xu, L. Lystrom, Y. Pan, X. Sun, S. A. Thomas, S. V. Kilina, Z. Yang, H. Wang, E. K. Hobbie, W. Sun, *Inorg. Chem.* **2021**, *60*, 15278; c) Z. Zhang, Z. Wei, J. Guo, J. X. Lyu, B. Wang, G. Wang, C. Wang, L. Zhou, Z. Yuan, G. Xing, C. Wu, X. Zhang, *Nat. Commun.* **2024**, *15*, 170.

[13] a) C. E. McCusker, D. Hablot, R. Ziessel, F. N. Castellano, *Inorg. Chem.* **2014**, *53*, 12564; b) S. Goswami, R. W. Winkel, E. Alarousu, I. Ghiviriga, O. F. Mohammed, K. S. Schanze, *J. Phys. Chem. A.* **2014**, *118*, 11735.

[14] M. B. Zerdan, T. Ghorayeb, F. Saliba, S. Allam, M. B. Zerdan, M. Yaghi, N. Bilani, R. Jaafar, Z. Nahleh, *Cancers.* **2022**, *14*, 1253.

[15] J. A. Roque Iii, H. D. Cole, P. C. Barrett, L. M. Lifshits, R. O. Hodges, S. Kim, G. Deep, A. Frances-Monerris, M. E. Alberto, C. G. Cameron, S. A. McFarland, *J. Am. Chem. Soc.* **2022**, *144*, 8317.

[16] L. Zhou, F. Wei, J. Xiang, H. Li, C. Li, P. Zhang, C. Liu, P. Gong, L. Cai, K. Wong, *Chem. Sci.* **2020**, *11*, 12212.

[17] L. Liu, Z. Fan, Y. Tang, Z. Ke, *Clin. Exp. Res.* **2014**, *38*, 683.

[18] S. Etienne-Manneville, *Traffic.* **2004**, *5*, 470.
[19] M. A. Kluge, J. L. Fetterman, J. A. Vita, *Circ. Res.* **2013**, *112*, 1171.
[20] T. Li, Z. Xu, H. Chen, S. Zhen, H. Gu, Z. Zhao, B. Tang, *Chin. J. Chem. Eng.* **2023**, *468*, 143829.
[21] G. Wu, Y. Fang, S. Yang, J. R. Lupton, N. D. Turner, *J. Nutr.* **2004**, *134*, 489.
[22] X. Xiao, J. Sakamoto, M. Tanabe, S. Yamazaki, S. Yamabe, T. Matsumura-Inoue, *J. Electroanal. Chem.* **2002**, *527*, 33.
[23] L. R. R Santi, S. C. dos Santos, D. L. Novo, D. Bianchini, A. P. Gerola, G. Braga, W. Caetano, L. M. Moreira, E. L. Bastos, A. P. Romani, H. P. M. de Oliveira, *Dyes Pigm.* **2015**, *119*, 12.